ACS Energy LETTERS

http://pubs.acs.org/journal/aelccp

Fluorinated Superionic Oxychloride Solid Electrolytes for High-Voltage All-Solid-State Lithium Batteries

Yingjie Gao, Shumin Zhang, Feipeng Zhao, Jian Wang, Jigang Zhou, Weihan Li, Sixu Deng, Jiamin Fu, Xiaoge Hao, Ruying Li, and Xueliang Sun*

Cite This: ACS Energy Lett. 2024, 9, 1735−1742

Read Online

ACCESS | Metrics & More | Article Recommendations | Supporting Information

ABSTRACT: As the demand for higher energy density grows rapidly, the development of high-voltage all-solid-state lithium batteries (ASSLBs) becomes essential. However, most existing solid electrolytes (SEs) are still incapable of stable operation at high voltages. Herein, we report a series of fluorinated lithium tantalum oxychlorides (LTOC-F) as amorphous SEs for high-voltage ASSLBs. The optimized LTOC-10%F SE exhibits remarkably improved high-voltage stability and a high ionic conductivity of 2.3 mS cm^{-1} at 25 °C. The ASSLB using an LCO cathode and LTOC-10%F SE achieves a high capacity of 180 mAh g^{-1} with a cutoff voltage of 4.5 V and high-capacity retention of 81% after 300 cycles. Furthermore, the underlying mechanisms for enhanced performance are identified as the intrinsically extended electrochemical window of SE and the in-situ-formed LiF-rich cathode-electrolyte interface (CEI). Overall, this work provides a fluorination strategy for high-voltage ASSLBs and also offers insights into the analysis of amorphous SEs and CEIs.

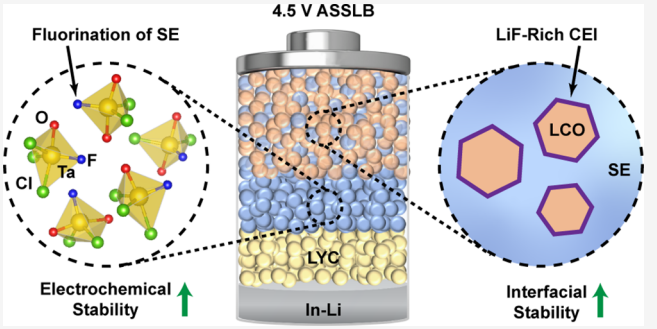

The global trend toward the electrification of transportation has posed challenges for traditional lithium-ion batteries (LIBs) in terms of safety, energy density, and operating temperature.[1] Unlike conventional LIBs, all-solid-state lithium batteries (ASSLBs) that employ nonflammable solid electrolytes (SEs) offer enhanced safety, the potential to use lithium metal as an anode, a wide operating temperature range, and reduced packaging requirements, making them a promising candidate for next-generation battery technology.[2−5] As the key component in ASSLBs, SEs have been taking center stage in this research field.[3] To date, some sulfide SEs (e.g., $Li_{10}GeP_2S_{12}$) have attained impressive high ionic conductivity exceeding 10 mS cm^{-1}, but most of them suffer from a narrow electrochemical window and incompatibility with prevalent cathode materials like $LiCoO_2$ (LCO).[5−16] To address these issues, a series of halide SEs have been developed, showing competitive ionic conductivity (>1 mS cm^{-1}) and good electrochemical stability with coating-free 4 V-class cathode materials.[17−23]

Despite these advances, the growing demand for higher energy density is driving the pursuit of higher working voltages. For example, conventional LCO cathodes can deliver only about 120 mAh g^{-1} when charged to 4.2 V, while modified high-voltage LCO cathodes can achieve about 180 mAh g^{-1} when charged to 4.5 V with an elevated average working voltage.[24,25] Unfortunately, most previously reported halide SEs could only provide a limited cutoff voltage of about 4.2−4.3 V vs Li^+/Li, since they would be oxidized, potentially forming metal chlorides and Cl_2 when the voltage exceeds this level.[22]

Theoretical calculations suggest that fluorides possess superior oxidation stability compared to other halides, oxides, and sulfides, with stability even exceeding 6 V vs Li^+/Li, as fluorine has the strongest electronegativity, which renders it resistant to oxidation.[26,27] Meanwhile, in situ formed fluorine-containing or fluorinated cathode-electrolyte interfaces (CEIs) are generally regarded as beneficial to high-voltage cathode materials due to their electrochemical stability and ability to transport Li^+ ions.[28−34] Therefore, fluorinating SEs has been

Received: October 19, 2023
Revised: March 8, 2024
Accepted: March 11, 2024
Published: March 25, 2024

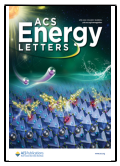

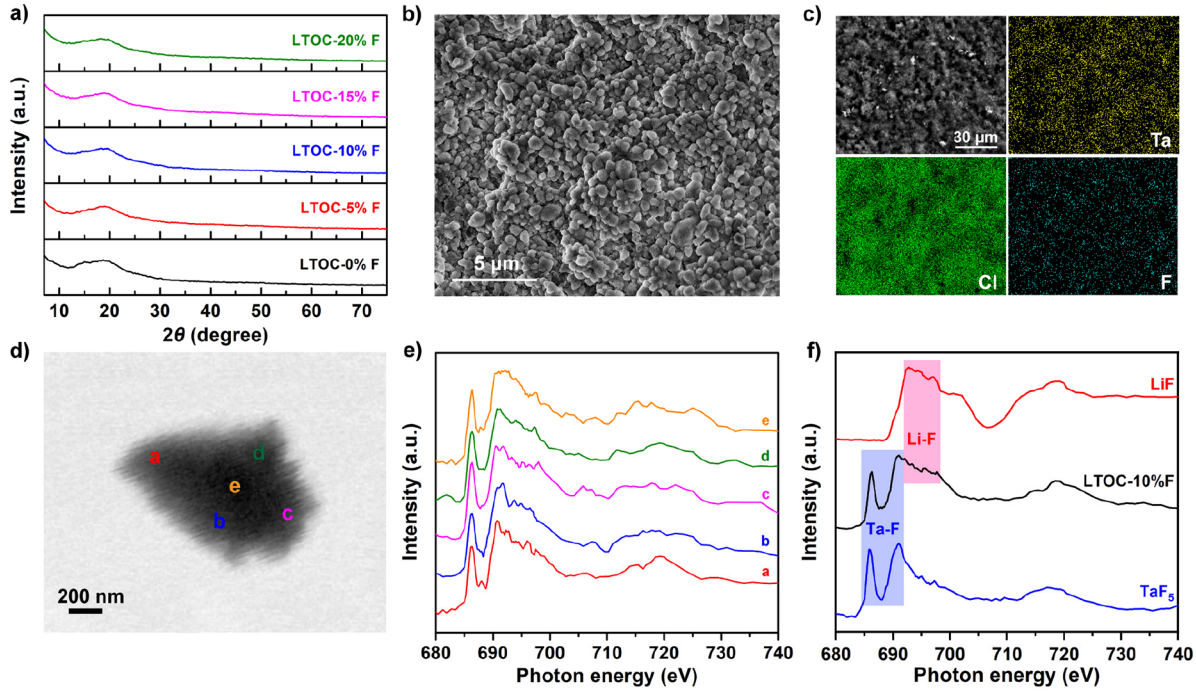

Figure 1. (a) XRD patterns of LTOC-*x*%F (x = 0, 5, 10, 15, and 20) SEs. (b) SEM image and (c) EDS mapping of Ta, Cl, and F elements of a cold-pressed pellet of LTOC-10%F SE. (d) STXM image of an LTOC-10%F SE particle at 690 eV. (e) F *K*-edge STXM XAS spectra at different regions (a−e) of the LTOC-10%F SE particle. (f) F *K*-edge bulk XAS spectra of the LTOC-10%F SE, LiF, and TaF_5.

regarded as a promising solution to stability issues, with several exploratory efforts having been made on various SEs.[33−41]

However, the fluorination of SEs consistently encounters challenges. Despite predictions that a few fluorides could exhibit high lithium-ion conductivity, no practical fluoride SEs have been developed to date.[42] Most reported fluoride SEs struggled with low ionic conductivity ($<10^{-2}$ mS cm^{-1}), possibly because of the strong ionic bonding between F^- and Li^+ ions that hinders the mobility of Li^+ ions in crystal structures.[22,43−45] Even the conductivities of those dual-halogen SEs partially doped with F^- ions dropped to an insufficient level of 10^{-1} mS cm^{-1}.[33,34,36−39] Moreover, although enhanced electrochemical stability was observed in some fluorinated ceramic SEs, the application of high-voltage cathodes such as 4.5 V LCO in ASSLBs with satisfactory performance has been rarely reported.[34,37]

Herein, we report a series of fluorinated superionic oxychloride electrolytes for high-voltage ASSLBs based on the recently developed amorphous nLi_2O-$TaCl_5$ (LTOC) SEs. The highly disordered local structures and the wide range of Li site distortions in LTOC SEs are expected to facilitate the chemical doping of F^- ions into the anion framework and provide adequate lithium-ion mobility post the fluorination.[46,47] As a result, the fluorinated SE with a substitution ratio of 10% (LTOC-10%F) showed a remarkable improvement in electrochemical stability toward high voltage while maintaining a high ionic conductivity of 2.3 mS cm^{-1}, which sets a new record in fluorinated SEs. The ASSLBs using coating-free high-voltage LCO cathodes and the LTOC-10%F SE achieved high performance in the voltage range of 2.6−4.5 V vs Li^+/Li, including a high capacity of 180 mAh g^{-1} and a good capacity retention of 81% after 300 cycles. Besides, the amorphous structure of SEs and the structure evolution induced by fluorination were studied by a variety of advanced characterization methods. The interface between the LCO cathode and the fluorinated SE LTOC-10%F was also investigated and visualized, revealing a LiF-rich interlayer.

The LTOC-*x*%F (x = 0, 5, 10, 15, and 20) SEs were synthesized by a ball-milling method based on the newly developed amorphous LTOC SEs, with Li_2O, $TaCl_5$, and TaF_5 powder at a ratio of 1.5:1-x:x used as raw materials.[46] All the as-synthesized LTOC-*x*%F (x = 0, 5, 10, 15, and 20) SEs were highly amorphous materials, as evidenced by the presence of only broad and weak peaks primarily attributed to Kapton sealing tapes in each lab-based powder X-ray diffraction (XRD) pattern (Figures 1a and S1). The further synchrotron-based XRD patterns (Figure S2) revealed that the SE samples also have wide peaks around 14°, implying the existence of some locally ordered structures. Interestingly, a minuscule amount of LiCl and Li_2O impurities were identified by synchrotron XRD, and the intensity of their signals increased along with a small left shift of the wide peak in the pattern of LTOC-20%F. It meant the 20% ratio might be close to the limit of doping. The scanning electron microscope (SEM) images of the fluorinated SEs (Figures 1b and S3) further disclosed their microscopic morphology that consisted of irregular nanoparticles to microparticles and a decreasing trend in average particle size as the degree of fluorination increased, potentially resulting in a denser cold-pressed pellet with lower porosity (Figure S4).[34,48] The energy dispersive spectroscopy (EDS) elemental mapping images (Figure 1c) that clearly displayed the uniform distribution of Ta, Cl, and F proved that the SEs were chemically fluorinated rather than physically mixed with fluorides. The scanning transmission X-ray microscopy (STXM) technique was then employed to investigate a single SE particle (Figure 1d). We found that the F *K*-edge X-ray absorption spectroscopy (XAS) spectra at regions a−e of the LTOC-10%F SE particle showed good consistency (Figure 1e), providing convincing evidence of the uniform fluorine substitution in the chemical structure.

https://doi.org/10.1021/acsenergylett.3c02243
ACS Energy Lett. 2024, 9, 1735−1742

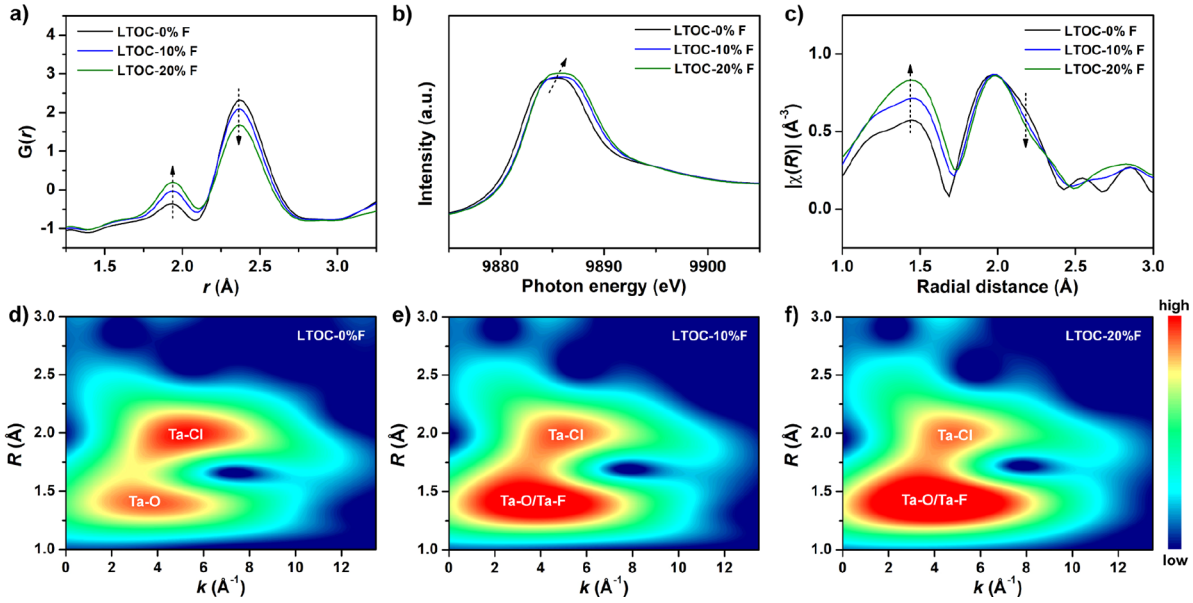

Figure 2. (a) PDF analysis, (b) Ta L_3-edge XANES spectra, and (c) k^2-weighted EXAFS spectra in the R space of fluorinated LTOC SEs with different doping ratios; wavelet transformed EXAFS spectra of (d) LTOC-0%F, (e) LTOC-10%F, and (f) LTOC-20%F. The R range was set as 1−3 Å, and the k weight was 2. The Morlet wavelet was employed for the calculation. The color mapping from blue to red was used to represent the magnitude of the wavelet coefficient from low to high.

Moreover, the F K-edge bulk XAS spectrum of the fluorinated SE exhibited characters of both LiF and TaF_5 reference samples (Figure 1f). The pre-edge feature at 686.1 eV in the spectrum of TaF_5 was assigned to the transitions from F 1s to the mixing state of F 2p and Ta 5d.[49] It was retained in the spectrum of LTOC-10%F, suggesting the Ta−F hybridization still existed in the fluorinated SE. On the other hand, the features in the range of 692.8−698.3 eV of LTOC-10%F were inconsistent with those of TaF_5 but agreed with the features of LiF. Therefore, the coexistence of Li−F bonding and Ta−F bonding was confirmed in the structure of LTOC-10%F SE.

Furthermore, the local structures of the glassy LTOC-x%F SEs were investigated by pair distribution function (PDF), X-ray absorption near edge structure (XANES), and extended X-ray absorption fine structure (EXAFS). The peaks representing Ta/Li−O and Ta/Li−F bonds at ∼1.9 Å and the peaks representing Ta/Li−Cl bonds at ∼2.4 Å became stronger and weaker, respectively, with increasing fluorination in PDF, demonstrating the substitution of chlorine by fluorine in the structure (Figure 2a). As the fluorine proportion increased in the LTOC-x%F SEs, the rising edge feature in Ta L_3-edge XANES shifted to a higher photon energy with a slight enhancement of the intensity (Figure 2b). Concurrently, the first derivative absorption peaks of the LTOC-0%F, 10%F, and 20%F SEs were located at 9882.0, 9882.4, and 9882.6 eV respectively, showing a trend toward higher energy (Figure S5). This trend agreed with the difference among the $TaCl_5$, Ta_2O_5, and TaF_5 reference samples (Figure S6a,b). The right shift could be explained by the stronger electronegativity of fluorine compared to that of chlorine, and the slight increase of intensity corresponded to the feature of TaF_5. Additionally, the intensified peaks at ∼1.5 Å and the slightly attenuated peaks at ∼2.0 Å in EXAFS could be attributed to the increase of Ta−O/F paths and decrease of Ta−Cl paths, respectively (Figures 2c and S6c). To further distinguish between Ta−O and Ta−F paths, which are at very similar distances, the wavelet transformation was performed.[50,51] The Ta−F feature with stronger intensity in the higher k space was observed accordingly in the spectra of fluorinated SEs, verifying the presence of F atoms in the first shell of Ta atoms (Figures 2d−f and S7).[52,53] The semiquantitative EXAFS fitting results also supported the above inferences and revealed a rise in the total coordination number of Ta after fluorine doping (Figure S8 and Table S1). In the Cl K-edge XAS spectra, the Ta−Cl···Li features of LTOC SE were still preserved after fluorination, indicating that the coordination environment of Cl favorable for Li-ion transport was not disrupted (Figure S9).

Overall, F^- ions entered the anionic framework of the amorphous SEs with the replacement of equivalent amount of Cl^- ions, resulting in the emergence of Ta−F and Li−F bonds and the evolution of Ta-centered polyhedra in the local structure, which could improve the stability of SEs. Simultaneously, the bulk of the disordered structure persisted, along with an abundance of unsaturated Ta−Cl···Li bonds, potentially maintaining the lithium-ion mobility at a high level.[46]

The impact of fluorination on the electrochemical window was subsequently evaluated by linear sweep voltammetry (LSV) tests with SE/carbon composites as working electrodes (Figures 3a and S10).[54] It was clear that the anodic peak was remarkably weakened as more fluorine was introduced into the SEs. For the LTOC-x%F ($x \geq 10$) SEs, their anodic peaks were even imperceptible compared to that of the original LTOC SE. Furthermore, we calculated the integral area under the LSV curves to qualitatively describe the degree of the decomposition side reaction. As shown in Figures 3b and S11, there was a growing tendency in both the onset potentials and the anodic peak potentials (E_{pa}) and an opposite one in the area under the LSV curves, indicating the fluorinated strategy is effective in improving high-voltage stability. Besides, the room-temperature ionic conductivities of the LTOC-x%F (x = 0, 5, 10, 15, or 20) SEs were determined using EIS measurements (Figure 3c). Although fluorine doping usually has a negative influence on the ionic conductivity, the LTOC-x%F SEs here

https://doi.org/10.1021/acsenergylett.3c02243
ACS Energy Lett. 2024, 9, 1735−1742

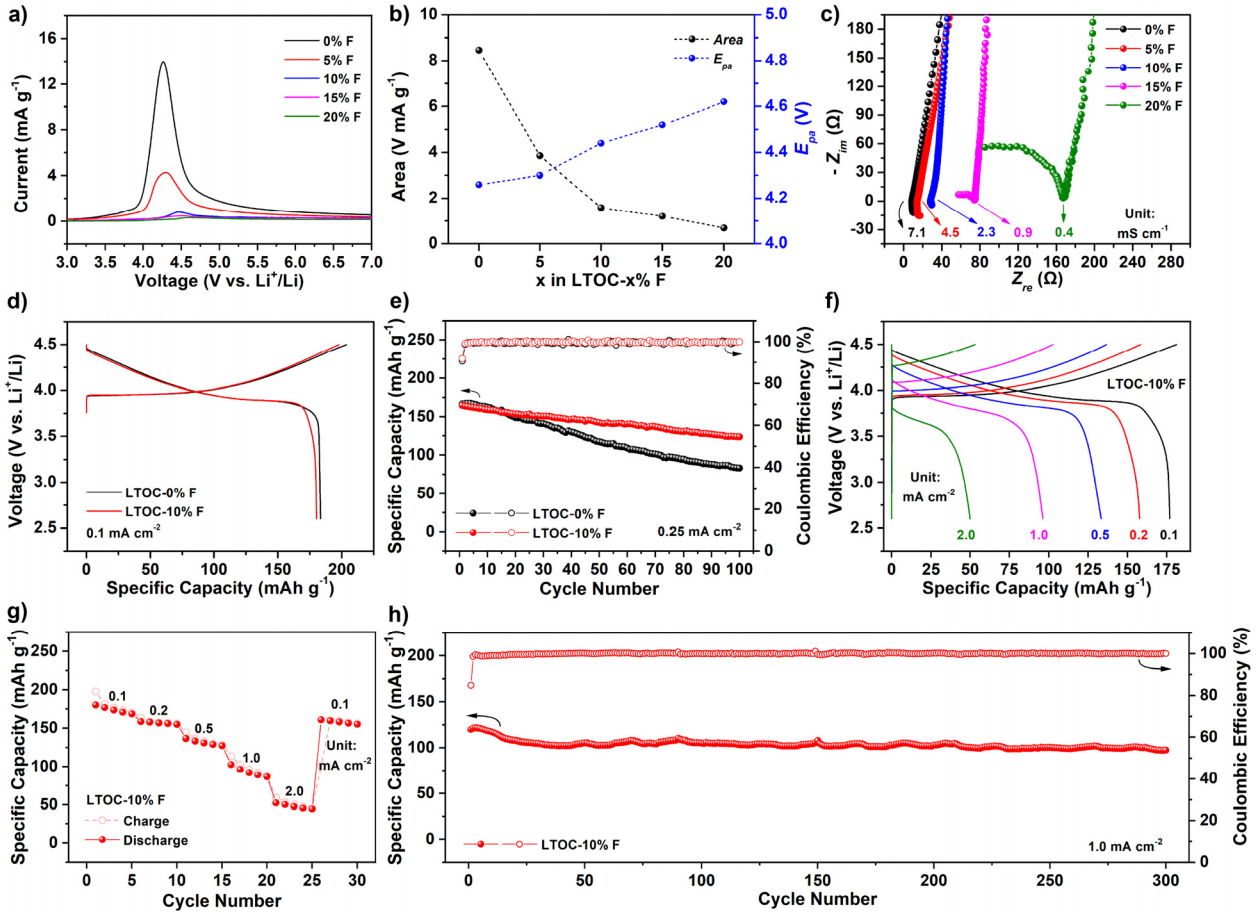

Figure 3. (a) LSV curves of the fluorinated LTOC SEs with different doping ratios at 0.1 mV s^{-1}. (b) The corresponding areas of the regions under the LSV curves and the anodic peak potentials (E_{pa}); the dotted lines are guides for the eye. (c) Nyquist plots of the fluorinated LTOC SEs with different doping ratios and the corresponding ionic conductivities at room temperature. (d) Voltage curves of the LCO cathode with LTOC-0%F and LTOC-10%F SEs in the first cycle at 0.1 mA cm^{-2}. (e) Cycling performance of the LCO cathode with LTOC-0%F and LTOC-10%F SEs at 0.25 mA cm^{-2}. (f) Voltage curves of the LCO cathode with LTOC-10%F SE at different rates. (g) The corresponding cycling performance at different rates. (h) Long-term cycling performance of the LCO cathode with LTOC-10%F SE at 1.0 mA cm^{-2}.

still showed acceptable ionic conductivities (>0.4 mS cm^{-1}).[22,43−45] The activation energies (E_a) of these SE materials were found to be 0.28−0.35 eV based on the temperature-dependent EIS results (Figure S12). The minute growth in activation energy matched up with the moderate loss of ionic conductivity and indicated that the favorable lithium-ion transport paths were possibly retained in the fluorinated SEs.

Taking the ionic conductivity and electrochemical stability into consideration together, the LTOC-10%F SE was selected as the optimized sample to fabricate high-voltage ASSLBs with LCO cathodes. In the voltage range of 2.6 to 4.5 V vs Li^+/Li, the LCO cathode with LTOC-0%F SE delivered 183.4 mAh g^{-1} with an initial Coulombic efficiency (CE) of 90.0% at 0.1 mA cm^{-2} (0.1 mA cm^{-2} ≈ 0.1 C). By comparison, the LCO cathode with the LTOC-10%F SE delivered a similar capacity of 180.2 mAh g^{-1} but with a higher initial CE of 91.1% (Figure 3d). The high capacity was contributed by LTOC-10%F's high ionic conductivity (2.3 mS cm^{-1}), and the superior initial CE could be explained by the less decomposition side reactions of SEs. The cycling performance at a moderate current rate of 0.25 mA cm^{-2} also demonstrated the advantage of LTOC-10% F SE (Figure 3e). The capacity retention of the LCO cathode with LTOC-0%F SE was only 50%, but it markedly rose to 75% when using the LTOC-10%F SE. Similarly, the ASSLBs using LTOC-20%F SE showed distinct improvement on the cycling stability as well (Figure S13). Moreover, the LTOC-10%F SE could provide an acceptable rate performance for ASSLBs (Figure 3f). The ASSLBs released capacities of 177, 158, 133, and 96 mAh g^{-1} under increased current rates of 0.1, 0.2, 0.5, and 1.0 mA cm^{-2}, respectively. When the current returned to a small density of 0.1 mA cm^{-2}, the reversible capacity recovered as well (Figure 3g). At the current rate of 1.0 mA cm^{-2}, the ASSLBs using LTOC-10%F SE charged to 4.5 V achieved excellent long-term cycling performance including a notable capacity retention of 81% and a high average CE of 99.9% (Figure 3h). In light of the above, the fluorinated LTOC-10%F SE exhibited superior comprehensive performance compared to the previously reported high-voltage ceramic SEs in terms of ionic conductivity, intrinsic electrochemical stability, and cycling stability and capacity of the ASSLBs (Table S2).

Beyond the electrochemical stability of SEs, a favorable CEI is also a critical factor in achieving high-performance ASSLBs. The EIS data of an ASSLB utilizing an LCO cathode and LTOC-10%F SE were gathered in the initial charge and discharge cycles (Figure 4a). During the charging process, the cathode-related resistance (colored in yellow) first remained

https://doi.org/10.1021/acsenergylett.3c02243
ACS Energy Lett. 2024, 9, 1735−1742

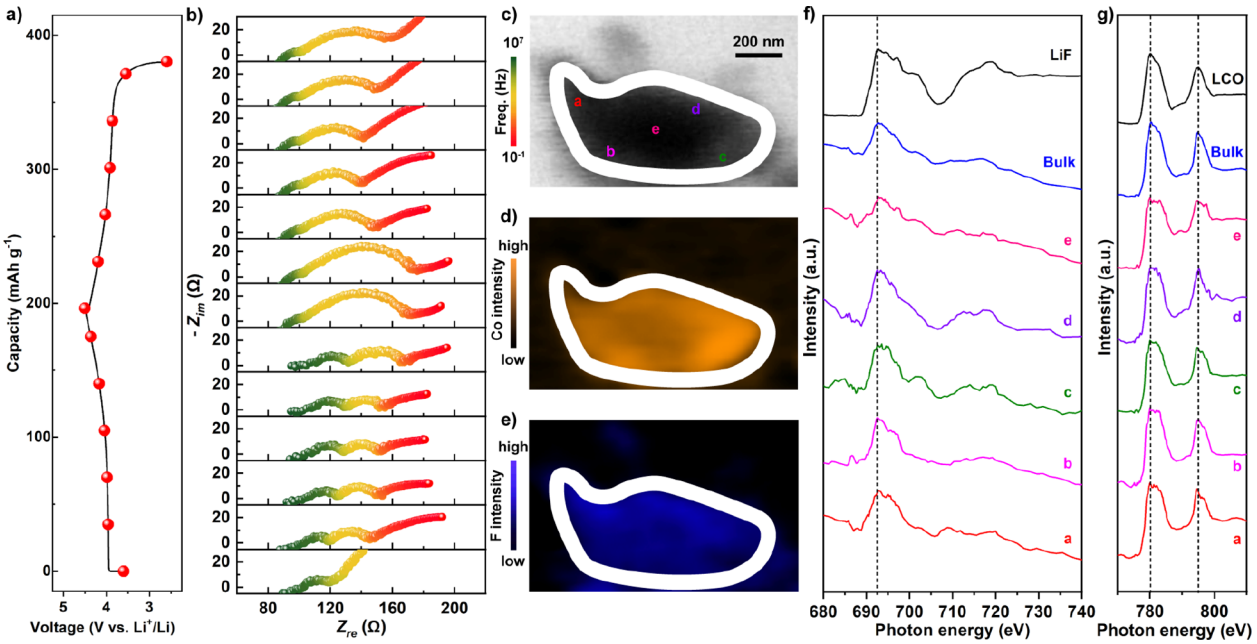

Figure 4. (a) Voltage curves of the LCO cathode with LTOC-10%F SEs in the first cycle. The red balls indicate the measurements of EIS. (b) The corresponding in situ EIS spectra of the full cell. (c) STXM image at 690 eV, (d) the corresponding Co mapping, and (e) the corresponding F mapping of an LCO cathode particle after cycling using LTOC-10%F as SE. The white lines are guides for the eye. (f) STXM F *K*-edge and Co $L_{2,3}$-edges XAS spectra of the different regions (a−e) on the LCO cathode particle with LiF and pristine LCO as reference samples.

steady at around 20 Ω, signaling good compatibility between the LCO active material and the LTOC-10%F SE.[17,18,55,56] Upon reaching a high voltage of 4.5 V, the cathode-related resistance slightly increased to around 60 Ω and remained relatively stable in the subsequent discharge process (Figure 4b). This could partially be ascribed to the evolution of the contact between cathode and SE upon deep deintercalation of lithium and also implied the formation of a stable CEI.[18,56] The second and third LSV curves of LTOC-10%F SE showed significantly reduced current densities and nearly linear behaviors, agreeing with the deduction that the passivating interface was in situ generated during the initial charging process (Figure S14). Furthermore, an LCO cathode particle after cycling with LTOC-10%F SE was studied by STXM (Figure 4c). The strong signal of cobalt across the entire particle eliminated the possibility of it being an SE particle (Figure 4d). Subsequent STXM F mapping on the same particle clearly indicated that the LCO cathode was covered by a F-containing CEI after cycling (Figure 4e). The consistency of these XANES spectra at different points demonstrated the homogeneity of this CEI layer (Figure 4f). The similarity between all of the rising edge features of a−e and the entire region to that of LiF revealed that the CEI was LiF-rich. In parallel, the uniformity of the cathode redox reaction after cycling was verified by the Co $L_{2,3}$-edge XAS spectra of bulk and different points on the particle, suggesting the advantageous function of the CEI (Figure 4g). Besides, the Co XAS spectra of the LCO cathode with varying cycle numbers were also collected, and their features were in line with the pristine one (Figure S15). Therefore, we could speculate that the LiF-rich CEI in situ formed on the surface of LCO cathode, which served to protect the cathode from further side reactions and deterioration at high voltages.

In summary, a series of fluorinated oxychloride LTOC-*x*%F SEs were successfully synthesized by a ball-milling method. The fluorine was confirmed to be introduced into the amorphous structure with the formation of Ta−F and Li−F bonding. The evolution of the coordination environment surrounding Ta atoms was investigated in detail, and the increase in Ta−F bonding and total coordination number with a slight reduction in Ta−Cl and Ta−O bonding were observed. The fluorinated SE LTOC-10%F showed a remarkable improvement on the electrochemical stability toward high voltage, and it still had a high ionic conductivity of 2.3 mS cm^{-1} at the same time. The ASSLBs using the LCO cathode and LTOC-10%F SE achieved high performance in terms of specific capacity, rate performance, and cycling stability. Besides, the mechanisms for the superior performance were concluded to be the intrinsically extended electrochemical window and the in situ formed LiF-rich CEI that could further protect the cathode. We believe this work not only proposed and achieved a fluorinating strategy for high-voltage ASSLBs but also provided deep insights into the analysis of SE's amorphous structure and the interface between SEs and electrodes.

■ ASSOCIATED CONTENT

Supporting Information

The Supporting Information is available free of charge at https://pubs.acs.org/doi/10.1021/acsenergylett.3c02243.

Experimental procedures, additional XRD, SEM, XANES, EXAFS, Nyquist plots, and electrochemical data (PDF)

■ AUTHOR INFORMATION

Corresponding Author

Xueliang Sun − *Department of Mechanical and Materials Engineering, University of Western Ontario, London, Ontario N6A 5B9, Canada; Eastern Institute for Advanced Study,*

https://doi.org/10.1021/acsenergylett.3c02243
ACS Energy Lett. 2024, 9, 1735−1742

Eastern Institute of Technology, Ningbo, Zhejiang 315200, P.R. China; orcid.org/0000-0003-0374-1245; Email: xsun9@uwo.ca

Authors

Yingjie Gao − *Department of Mechanical and Materials Engineering, University of Western Ontario, London, Ontario N6A 5B9, Canada;* orcid.org/0000-0002-6853-7870

Shumin Zhang − *Department of Mechanical and Materials Engineering, University of Western Ontario, London, Ontario N6A 5B9, Canada*

Feipeng Zhao − *Department of Mechanical and Materials Engineering, University of Western Ontario, London, Ontario N6A 5B9, Canada*

Jian Wang − *Canadian Light Source Inc., University of Saskatchewan, Saskatoon, Saskatchewan S7N 2V3, Canada*

Jigang Zhou − *Canadian Light Source Inc., University of Saskatchewan, Saskatoon, Saskatchewan S7N 2V3, Canada;* orcid.org/0000-0001-6644-2862

Weihan Li − *Department of Mechanical and Materials Engineering, University of Western Ontario, London, Ontario N6A 5B9, Canada*

Sixu Deng − *Department of Mechanical and Materials Engineering, University of Western Ontario, London, Ontario N6A 5B9, Canada;* orcid.org/0000-0001-7458-0296

Jiamin Fu − *Department of Mechanical and Materials Engineering, University of Western Ontario, London, Ontario N6A 5B9, Canada*

Xiaoge Hao − *Department of Mechanical and Materials Engineering, University of Western Ontario, London, Ontario N6A 5B9, Canada*

Ruying Li − *Department of Mechanical and Materials Engineering, University of Western Ontario, London, Ontario N6A 5B9, Canada*

Complete contact information is available at: https://pubs.acs.org/10.1021/acsenergylett.3c02243

Notes

The authors declare no competing financial interest.

■ ACKNOWLEDGMENTS

This research was supported by the Natural Sciences and Engineering Research Council of Canada (NSERC), the Canada Research Chair Program (CRC), the Canada Foundation for Innovation (CFI), Ontario Research Foundation (ORF), China Automotive Battery Research Institute Co., Ltd., Glabat Solid-State Battery Inc., and the University of Western Ontario (UWO). The synchrotron research was performed at the SM, HXMA, BXDS-WHE, and SXRMB beamlines of the Canadian Light Source (CLS), a national research facility of the University of Saskatchewan, which was supported by the CFI, NSERC, the National Research Council (NRC), the Canadian Institutes of Health Research (CIHR), the Government of Saskatchewan, and the University of Saskatchewan. The authors also gratefully acknowledge Dr. Ning Chen, Dr. Graham King, and Dr. Mohsen Shakouri for their great help at the CLS. Mr. Yingjie Gao and Dr. Weihan Li acknowledge the receipt of support from the CLSI Graduate and Post-Doctoral Student Travel Support Program. Dr. Weihan Li appreciates the funding support from Mitacs Accelerate Fellowships.

■ REFERENCES

(1) Hu, Y. S. Batteries: getting solid. *Nat. Energy* **2016**, *1*, 16042.
(2) Zhang, Z.; Shao, Y.; Lotsch, B.; Hu, Y. S.; Li, H.; Janek, J.; Nazar, L. F.; Nan, C. W.; Maier, J.; Armand, M.; Chen, L. New horizons for inorganic solid state ion conductors. *Energy Environ. Sci.* **2018**, *11*, 1945.
(3) Chen, R.; Li, Q.; Yu, X.; Chen, L.; Li, H. Approaching practically accessible solid-state batteries: stability issues related to solid electrolytes and interfaces. *Chem. Rev.* **2020**, *120*, 6820−6877.
(4) Famprikis, T.; Canepa, P.; Dawson, J. A.; Islam, M. S.; Masquelier, C. Fundamentals of inorganic solid-state electrolytes for batteries. *Nat. Mater.* **2019**, *18*, 1278−1291.
(5) Kato, Y.; Hori, S.; Saito, T.; Suzuki, K.; Hirayama, M.; Mitsui, A.; Yonemura, M.; Iba, H.; Kanno, R. High-power all-solid-state batteries using sulfide superionic conductors. *Nat. Energy* **2016**, *1*, 16030.
(6) Zhao, W.; Yi, J.; He, P.; Zhou, H. Solid-state electrolytes for lithium-ion batteries: fundamentals, challenges and perspectives. *Electrochem. Energy Rev.* **2019**, *2*, 574−605.
(7) Liu, Q.; Chen, Q.; Tang, Y.; Cheng, H. M. Interfacial Modification, Electrode/Solid-Electrolyte Engineering, and Monolithic Construction of Solid-State Batteries. *Electrochem. Energy Rev.* **2023**, *6*, 15.
(8) Kamaya, N.; Homma, K.; Yamakawa, Y.; Hirayama, M.; Kanno, R.; Yonemura, M.; Kamiyama, T.; Kato, Y.; Hama, S.; Kawamoto, K.; Mitsui, A. A lithium superionic conductor. *Nat. Mater.* **2011**, *10*, 682−686.
(9) Adeli, P.; Bazak, J. D.; Park, K. H.; Kochetkov, I.; Huq, A.; Goward, G. R.; Nazar, L. F. Boosting Solid-State Diffusivity and Conductivity in Lithium Superionic Argyrodites by Halide Substitution. *Angew. Chem., Int. Ed.* **2019**, *58*, 8681−8686.
(10) Wang, C.; Liang, J.; Zhao, Y.; Zheng, M.; Li, X.; Sun, X. All-solid-state lithium batteries enabled by sulfide electrolytes: from fundamental research to practical engineering design. *Energy Environ. Sci.* **2021**, *14*, 2577.
(11) Lu, P.; Wu, D.; Chen, L.; Li, H.; Wu, F. Air stability of solid-state sulfide batteries and electrolytes. *Electrochem. Energy Rev.* **2022**, *5*, 3.
(12) Sakuda, A.; Hayashi, A.; Tatsumisago, M. Interfacial Observation between $LiCoO_2$ Electrode and Li_2S-P_2S_5 Solid Electrolytes of All-Solid-State Lithium Secondary Batteries Using Transmission Electron Microscopy. *Chem. Mater.* **2010**, *22*, 949−956.
(13) Han, F.; Zhu, Y.; He, X.; Mo, Y.; Wang, C. Electrochemical stability of $Li_{10}GeP_2S_{12}$ and $Li_7La_3Zr_2O_{12}$ solid electrolytes. *Adv. Energy Mater.* **2016**, *6*, 1501590.
(14) Koerver, R.; Aygün, I.; Leichtweiß, T.; Dietrich, C.; Zhang, W.; Binder, J. O.; Hartmann, P.; Zeier, W. G.; Janek, J. Capacity fade in solid-state batteries: interphase formation and chemomechanical processes in nickel-rich layered oxide cathodes and lithium thiophosphate solid electrolytes. *Chem. Mater.* **2017**, *29*, 5574−5582.
(15) Auvergniot, J.; Cassel, A.; Ledeuil, J. B.; Viallet, V.; Seznec, V.; Dedryvère, R. Interface stability of argyrodite Li_6PS_5Cl toward $LiCoO_2$, $LiNi_{1/3}Co_{1/3}Mn_{1/3}O_2$, and $LiMn_2O_4$ in bulk all-solid-state batteries. *Chem. Mater.* **2017**, *29*, 3883−3890.
(16) Walther, F.; Koerver, R.; Fuchs, T.; Ohno, S.; Sann, J.; Rohnke, M.; Zeier, W. G.; Janek, J. Visualization of the interfacial decomposition of composite cathodes in argyrodite-based all-solid-state batteries using time-of-flight secondary-ion mass spectrometry. *Chem. Mater.* **2019**, *31*, 3745−3755.
(17) Asano, T.; Sakai, A.; Ouchi, S.; Sakaida, M.; Miyazaki, A.; Hasegawa, S. Solid halide electrolytes with high lithium-ion conductivity for application in 4 V class bulk-type all-solid-state batteries. *Adv. Mater.* **2018**, *30*, 1803075.
(18) Li, X.; Liang, J.; Luo, J.; Norouzi Banis, M.; Wang, C.; Li, W.; Deng, S.; Yu, C.; Zhao, F.; Hu, Y.; et al. Air-stable Li_3InCl_6 electrolyte with high voltage compatibility for all-solid-state batteries. *Energy Environ. Sci.* **2019**, *12*, 2665−2671.
(19) Wang, K.; Ren, Q.; Gu, Z.; Duan, C.; Wang, J.; Zhu, F.; Fu, Y.; Hao, J.; Zhu, J.; He, L.; Wang, C. W.; et al. A cost-effective and

humidity-tolerant chloride solid electrolyte for lithium batteries. *Nat. Commun.* **2021**, *12*, 4410.
(20) Liang, J.; Li, X.; Adair, K. R.; Sun, X. Metal halide superionic conductors for all-solid-state batteries. *Acc. Chem. Res.* **2021**, *54*, 1023−1033.
(21) Zhou, L.; Zuo, T. T.; Kwok, C. Y.; Kim, S. Y.; Assoud, A.; Zhang, Q.; Janek, J.; Nazar, L. F. High areal capacity, long cycle life 4 V ceramic all-solid-state Li-ion batteries enabled by chloride solid electrolytes. *Nat. Energy* **2022**, *7*, 83−93.
(22) Li, X.; Liang, J.; Yang, X.; Adair, K. R.; Wang, C.; Zhao, F.; Sun, X. Progress and perspectives on halide lithium conductors for all-solid-state lithium batteries. *Energy Environ. Sci.* **2020**, *13*, 1429.
(23) Tanaka, Y.; Ueno, K.; Mizuno, K.; Takeuchi, K.; Asano, T.; Sakai, A. New Oxyhalide Solid Electrolytes with High Lithium Ionic Conductivity > 10 mS cm^{-1} for All-Solid-State Batteries. *Angew. Chem., Int. Ed.* **2023**, *62*, No. e202217581.
(24) Liu, Q.; Su, X.; Lei, D.; Qin, Y.; Wen, J.; Guo, F.; Wu, Y. A.; Rong, Y.; Kou, R.; Xiao, X.; Aguesse, F.; et al. Approaching the capacity limit of lithium cobalt oxide in lithium ion batteries via lanthanum and aluminium doping. *Nat. Energy* **2018**, *3*, 936−943.
(25) Zhang, J. N.; Li, Q.; Ouyang, C.; Yu, X.; Ge, M.; Huang, X.; Hu, E.; Ma, C.; Li, S.; Xiao, R.; Yang, W.; et al. Trace doping of multiple elements enables stable battery cycling of $LiCoO_2$ at 4.6 V. *Nat. Energy* **2019**, *4*, 594−603.
(26) Richards, W. D.; Miara, L. J.; Wang, Y.; Kim, J. C.; Ceder, G. Interface stability in solid-state batteries. *Chem. Mater.* **2016**, *28*, 266−273.
(27) Wang, S.; Bai, Q.; Nolan, A. M.; Liu, Y.; Gong, S.; Sun, Q.; Mo, Y. Lithium chlorides and bromides as promising solid-state chemistries for fast ion conductors with good electrochemical stability. *Angew. Chem., Int. Ed.* **2019**, *58*, 8039−8043.
(28) Banerjee, A.; Wang, X.; Fang, C.; Wu, E. A.; Meng, Y. S. Interfaces and interphases in all-solid-state batteries with inorganic solid electrolytes. *Chem. Rev.* **2020**, *120*, 6878−6933.
(29) Xiao, Y.; Wang, Y.; Bo, S. H.; Kim, J. C.; Miara, L. J.; Ceder, G. Understanding interface stability in solid-state batteries. *Nat. Rev. Mater.* **2020**, *5*, 105−126.
(30) Zhang, Q. Fluorinated interphases. *Nat. Nanotechnol.* **2018**, *13*, 623−624.
(31) Culver, S. P.; Koerver, R.; Zeier, W. G.; Janek, J. On the functionality of coatings for cathode active materials in thiophosphate-based all-solid-state batteries. *Adv. Energy Mater.* **2019**, *9*, 1900626.
(32) Fan, X.; Ji, X.; Han, F.; Yue, J.; Chen, J.; Chen, L.; Deng, T.; Jiang, J.; Wang, C. Fluorinated solid electrolyte interphase enables highly reversible solid-state Li metal battery. *Sci. Adv.* **2018**, *4*, No. eaau9245.
(33) Zhao, F.; Sun, Q.; Yu, C.; Zhang, S.; Adair, K.; Wang, S.; Liu, Y.; Zhao, Y.; Liang, J.; Wang, C.; Li, X.; et al. Ultrastable anode interface achieved by fluorinating electrolytes for all-solid-state Li metal batteries. *ACS Energy Lett.* **2020**, *5*, 1035−1043.
(34) Zhang, S.; Zhao, F.; Wang, S.; Liang, J.; Wang, J.; Wang, C.; Zhang, H.; Adair, K.; Li, W.; Li, M.; Duan, H.; Zhao, Y.; Yu, R.; Li, R.; Huang, H.; Zhang, L.; Zhao, S.; Lu, S.; Sham, T.-K.; Mo, Y.; Sun, X. Advanced high-voltage all-solid-state Li-ion batteries enabled by a dual-halogen solid electrolyte. *Adv. Energy Mater.* **2021**, *11*, 2100836.
(35) Yu, T.; Liang, J.; Luo, L.; Wang, L.; Zhao, F.; Xu, G.; Bai, X.; Yang, R.; Zhao, S.; Wang, J.; et al. Superionic fluorinated halide solid electrolytes for highly stable Li-metal in all-solid-state li batteries. *Adv. Energy Mater.* **2021**, *11*, 2101915.
(36) Umeshbabu, E.; Maddukuri, S.; Hu, Y.; Fichtner, M.; Munnangi, A. R. Influence of chloride ion substitution on lithium-ion conductivity and electrochemical stability in a dual-halogen solid-state electrolyte. *ACS Appl. Mater. Interfaces* **2022**, *14*, 25448−25456.
(37) Luo, X.; He, X.; Su, H.; Zhong, Y.; Wang, X.; Tu, J. Effective regulation towards electrochemical stability of superionic solid electrolyte via facile dual-halogen strategy. *J. Chem. Eng.* **2023**, *465*, 143036.
(38) Li, Y.; Zhou, W.; Xin, S.; Li, S.; Zhu, J.; Lü, X.; Cui, Z.; Jia, Q.; Zhou, J.; Zhao, Y.; Goodenough, J. B. Fluorine-doped antiperovskite electrolyte for all-solid-state lithium-ion batteries. *Angew. Chem., Int. Ed.* **2016**, *55*, 9965−9968.
(39) Feng, W.; Zhu, L.; Dong, X.; Wang, Y.; Xia, Y.; Wang, F. Enhanced Moisture Stability of Lithium-Rich Antiperovskites for Sustainable All-Solid-State Lithium Batteries. *Adv. Mater.* **2023**, *35*, 2210365.
(40) Kwak, H.; Kim, J. S.; Han, D.; Kim, J. S.; Park, J.; Kwon, G.; Bak, S. M.; Heo, U.; Park, C.; Lee, H. W.; et al. Boosting the interfacial superionic conduction of halide solid electrolytes for all-solid-state batteries. *Nat. Commun.* **2023**, *14*, 2459.
(41) Kim, S.; Lee, Y.; Kim, K.; Wood, B. C.; Han, S. S.; Yu, S. Fluorine-Substituted Lithium Chloride Solid Electrolytes for High-Voltage All-Solid-State Lithium-Ion Batteries. *ACS Energy Lett.* **2024**, *9*, 38−47.
(42) Liu, J.; Wang, S.; Qie, Y.; Sun, Q. Identifying lithium fluorides for promising solid-state electrolyte and coating material of high-voltage cathode. *Mater. Today Energy* **2021**, *21*, 100719.
(43) Esaka, T.; Okuyama, R.; Iwahara, H. Ionic conduction in sintered fluorocomplexes $LimMF_6$, M = Al, Ti. *Solid State Ion.* **1989**, *34*, 201−205.
(44) Sorokin, N. I.; Karimov, D. N.; Komar'kova, O. N. Electrophysical properties of $LiYbF_4$ crystals. *Crystallogr. Rep.* **2010**, *55*, 448−449.
(45) Feinauer, M.; Euchner, H.; Fichtner, M.; Reddy, M. A. Unlocking the potential of fluoride-based solid electrolytes for solid-state lithium batteries. *ACS Appl. Energy Mater.* **2019**, *2*, 7196−7203.
(46) Zhang, S.; Zhao, F.; Chen, J.; Fu, J.; Luo, J.; Alahakoon, S. H.; Chang, L. Y.; Feng, R.; Shakouri, M.; Liang, J.; Zhao, Y.; et al. A family of oxychloride amorphous solid electrolytes for long-cycling all-solid-state lithium batteries. *Nat. Commun.* **2023**, *14*, 3780.
(47) Chandra, A.; Bhatt, A.; Chandra, A. Ion conduction in superionic glassy electrolytes: an overview. *J. Mater. Sci. Technol.* **2013**, *29*, 193−208.
(48) Ohsaki, S.; Yano, T.; Hatada, A.; Nakamura, H.; Watano, S. Size control of sulfide-based solid electrolyte particles through liquid-phase synthesis. *Powder Technol.* **2021**, *387*, 415−420.
(49) Roesch, P.; Vogel, C.; Huthwelker, T.; Wittwer, P.; Simon, F. G. Investigation of per-and polyfluoroalkyl substances (PFAS) in soils and sewage sludges by fluorine K-edge XANES spectroscopy and combustion ion chromatography. *Environ. Sci. Pollut. Res.* **2022**, *29*, 26889−26899.
(50) Funke, H.; Scheinost, A. C.; Chukalina, M. Wavelet analysis of extended x-ray absorption fine structure data. *Phys. Rev. B* **2005**, *71*, 094110.
(51) Funke, H.; Chukalina, M.; Scheinost, A. C. A new FEFF-based wavelet for EXAFS data analysis. *J. Synchrotron Rad.* **2007**, *14*, 426−432.
(52) Fei, H.; Dong, J.; Arellano-Jiménez, M. J.; Ye, G.; Dong Kim, N.; Samuel, E. L.; Peng, Z.; Zhu, Z.; Qin, F.; Bao, J.; et al. Atomic cobalt on nitrogen-doped graphene for hydrogen generation. *Nat. Commun.* **2015**, *6*, 8668.
(53) Ji, S.; Chen, Y.; Fu, Q.; Chen, Y.; Dong, J.; Chen, W.; Li, Z.; Wang, Y.; Gu, L.; He, W.; et al. Confined pyrolysis within metal-organic frameworks to form uniform Ru3 clusters for efficient oxidation of alcohols. *J. Am. Chem. Soc.* **2017**, *139*, 9795−9798.
(54) Schwietert, T. K.; Arszelewska, V. A.; Wang, C.; Yu, C.; Vasileiadis, A.; de Klerk, N. J.; Hageman, J.; Hupfer, T.; Kerkamm, I.; Xu, Y.; et al. Clarifying the relationship between redox activity and electrochemical stability in solid electrolytes. *Nat. Mater.* **2020**, *19*, 428−435.
(55) Vadhva, P.; Hu, J.; Johnson, M. J.; Stocker, R.; Braglia, M.; Brett, D. J.; Rettie, A. J. Electrochemical impedance spectroscopy for all-solid-state batteries: Theory, methods and future outlook. *ChemElectroChem.* **2021**, *8*, 1930−1947.
(56) Zhang, W.; Weber, D. A.; Weigand, H.; Arlt, T.; Manke, I.; Schröder, D.; Koerver, R.; Leichtweiss, T.; Hartmann, P.; Zeier, W. G.; Janek, J. Interfacial processes and influence of composite cathode

https://doi.org/10.1021/acsenergylett.3c02243
ACS Energy Lett. 2024, 9, 1735−1742

microstructure controlling the performance of all-solid-state lithium batteries. *ACS Appl. Mater. Interfaces* **2017**, *9*, 17835−17845.

https://doi.org/10.1021/acsenergylett.3c02243
ACS Energy Lett. 2024, 9, 1735−1742